

A Young, Low-Density Stellar Stream in the Milky Way Disk: Theia 456

JEFF J. ANDREWS,¹ JASON L. CURTIS,^{2,3} JULIO CHANAMÉ,⁴ MARCEL A. AGÜEROS,² SIMON C. SCHULER,⁵
MARINA KOUNKEL,⁶ AND KEVIN R. COVEY⁶

¹*Center for Interdisciplinary Exploration and Research in Astrophysics (CIERA), 1800 Sherman Ave., Evanston, IL 60201, USA*

²*Department of Astronomy, Columbia University, 550 West 120th Street, New York, NY 10027, USA*

³*American Museum of Natural History, 200 Central Park West, New York, NY 10024, USA*

⁴*Instituto de Astrofísica, Pontificia Universidad Católica de Chile, Av. Vicuña Mackenna 4860, 782-0436 Macul, Santiago, Chile*

⁵*University of Tampa, Department of Chemistry, Biochemistry, and Physics, Tampa, FL 33606, USA*

⁶*Department of Physics & Astronomy, Western Washington University, Bellingham, WA 98225-9164 USA*

Submitted to ApJ

ABSTRACT

Our view of the variety of stellar structures pervading the local Milky Way has been transformed by the application of clustering algorithms to the Gaia catalog. In particular, several stellar streams have been recently discovered that are comprised of hundreds to thousands of stars and span several hundred parsecs. We analyze one such structure, Theia 456, a low-density stellar stream extending nearly 200 pc and 20° across the sky. By supplementing Gaia astrometric data with spectroscopic metallicities from LAMOST and photometric rotation periods from the Zwicky Transient Facility (ZTF) and the Transiting Exoplanet Survey Satellite (TESS), we establish Theia 456’s radial velocity coherence, and we find strong evidence that members of Theia 456 have a common age ($\simeq 175$ Myr), common dynamical origin, and formed from chemically homogeneous pre-stellar material ($[\text{Fe}/\text{H}] = -0.07$ dex). Unlike well-known stellar streams in the Milky Way, which are in its halo, Theia 456 is firmly part of the thin disk. If our conclusions about Theia 456 can be applied to even a small fraction of the remaining $\simeq 8300$ independent structures in the Theia catalog, such low-density stellar streams may be ubiquitous. We comment on the implications this has for the nature of star-formation throughout the Galaxy.

1. INTRODUCTION

It is generally believed that most stars form in stellar clusters embedded within giant molecular clouds (cf. review in Lada & Lada 2003). However, many of these clusters are not massive enough to be bound, and only a minority of stars are formed within bound clusters, with the specific fraction dependent upon the definition of cluster used (Bressert et al. 2010). Some fraction of these stellar clusters may then survive for millions or even billions of years, as stellar associations, moving groups, and open clusters, but ultimately most stars disperse into the Milky Way field as single stars (Fall et al. 2005; Goodwin & Bastian 2006).

Studies of stellar populations in the Galaxy provide important constraints on the details of this scenario.

These studies have been revolutionized by the Gaia catalog, with its vastly improved astrometric precision and nearly two billion separately identified objects in its Early Data Release 3 (EDR3; Gaia Collaboration et al. 2021; Lindegren et al. 2021; Riello et al. 2021). In particular, researchers have uncovered new details about the population of Milky Way globular clusters (e.g., Vitral 2021), open clusters (e.g., Castro-Ginard et al. 2020), moving groups and young stellar associations (e.g., Ujjwal et al. 2020) stellar streams (e.g., Helmi 2020), and the origin of the Milky Way halo (e.g., Belokurov et al. 2018; Helmi et al. 2018).

Some of the most exciting discoveries have been produced by the application of modern statistical and machine learning algorithms to the Gaia data. For instance, using a combination of a wavelet decomposition technique and the unsupervised clustering algorithm DBSCAN, Meingast et al. (2019) discovered the Pisces–Eridanus/Meingast 1 stream, a nearly 400-pc-long structure comprised of 256 stars. Further stud-

ies by Ratzenböck et al. (2020) and Röser & Schilbach (2020) used support-vector machine and convergent point methods, respectively, to expand the number of member stars in this stream to over 10^3 .

Other recent, similar discoveries include that of Tian (2020), who identified a young (30–40 Myr), 200 pc long and 80 pc wide, stellar stream comprised of several thousand members. And Beccari et al. (2020) detected a 260-pc-long filamentary structure that links two previously known clusters, BBJ 1 and NGC 2547.

These discoveries may only be the tip of the iceberg. Kounkel & Covey (2019) and Kounkel et al. (2020) applied HDBSCAN (Campello et al. 2013; McInnes et al. 2017), a variation of DBSCAN, to the Gaia data release 2 (DR2; Gaia Collaboration et al. 2018; Lindegren et al. 2018). These authors’ Theia catalog, which extends to a distance of 3 kpc from the Sun, includes 8292 separate stellar structures, many of which are previously undetected, large, low-density filaments or streams, comprised of hundreds to thousands of stars and spanning hundreds of pc.

Whereas previously known stellar streams were all found within the Milky Way halo (e.g., Pal 5; Odenkirchen et al. 2001) and therefore the likely result of the tidal disruption of infalling satellite galaxies, these recently discovered structures exist within the Milky Way disk. As such, their origin is unclear. Both simulations (Renaud et al. 2013) and observations (van Loon et al. 2003) show that Galactic resonances produce overdensities in the Milky Way disk; these are collections of unassociated stars that happen to be caught within the same resonance. Alternatively, low-density stellar structures could have been formed from the same pre-stellar material, and we are observing them in the midst of dissipation (Kamdar et al. 2019).

Two follow-up studies of Pisces–Eridanus/Meingast 1 compared its properties to that of the benchmark Pleiades open cluster. Curtis et al. (2019) used rotation period measurements for stars in both structures to demonstrate that a large fraction of Pisces–Eridanus/Meingast 1 stars share a common age of ≈ 120 Myr, the age of the Pleiades. Hawkins et al. (2020) found that its stars have similar metallicity, and based on Li abundances, age, reinforcing the claim that they have a common origin. Follow-up observations such as these are critical to testing whether stars in these new structures share a common age and chemical origin, and therefore in elucidating their origin.

In this work, we assess the origin of another exciting, young, low-density stellar structure within the Milky Way disk, Theia 456. In Section 2, we demonstrate that after culling outliers, Theia 456 members have consis-

tent kinematics, metallicity, and age. We analyze the dynamical origin of Theia 456 in Section 3 by integrating orbits in a Milky Way potential. We discuss the implication our results have for star formation and Milky Way substructure in Section 4, and provide some concluding thoughts.

2. CHARACTERISTICS OF THEIA 456

To understand the structure and characteristics of Theia 456, we first analyze the Gaia EDR3 kinematics of candidate members identified by Kounkel & Covey (2019) in the Gaia DR2 catalog. After removing outliers, we provide an updated catalog of Theia 456 stars. We then cross-match the positions of these members with several additional catalogs: the Large Sky Area Multi-Object Fiber Spectroscopic Telescope (LAMOST) DR5 spectroscopic catalog (Cui et al. 2012; Luo et al. 2015), and the Transient Exoplanet Survey Satellite (TESS; Ricker et al. 2015), and Zwicky Transient Facility (ZTF; Bellm et al. 2019a,b) photometric databases.

Combined with astrometric, radial velocity, and photometric data from Gaia, these catalogs provide a complementary perspective which allows us to analyze the kinematic characteristics, metallicity, and age of Theia 456, each of which we describe in turn below.

2.1. Theia 456 Membership

We first start by updating the astrometric characteristics of the 468 reported members of Theia 456 identified by Kounkel & Covey (2019) to the latest Gaia EDR3 astrometric catalog from the original DR2 catalog. While the astrometric measurement precision for these stars improved between the two catalogs, we found the DR2 data to be quite accurate. In Figure 1 we provide a corner plot showing the EDR3 astrometric characteristics (proper motion Right Ascension, μ_α , and Declination, μ_δ , as well as parallaxes, ϖ) of the 468 candidate members identified by Kounkel & Covey (2019) as black points and histograms. With a typical precision $\lesssim 0.1$ mas in parallax and $\lesssim 0.1$ mas yr $^{-1}$ in proper motion, the scatter in the black points is larger than can be accounted for by measurement uncertainties, suggesting the initial catalog contains some contaminating stars.

To refine our catalog of Theia 456 members, we applied the unsupervised clustering algorithm DBSCAN to the three-dimensional astrometric data: μ_α , μ_δ , and ϖ . We use the implementation provided by `scikit-learn` (Pedregosa et al. 2011), with an `eps` value of 0.3, resulting in a refined catalog of 362 members. Although we found a value of 0.3 to be a good compromise between catalog size and purity, the resulting membership catalog depends quite strongly on the `eps` value

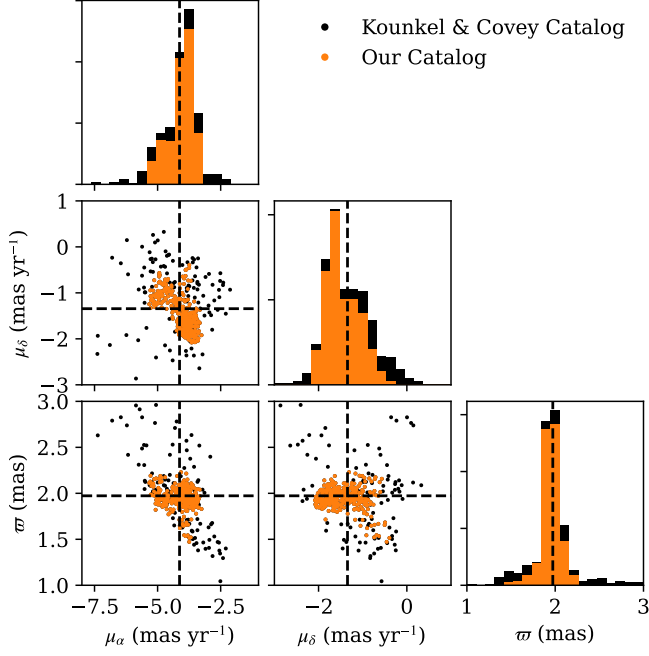


Figure 1. Gaia EDR3 astrometry for stars in the initial Kounkel & Covey (2019) catalog of candidate Theia 456 members (black) and our updated catalog (orange), in which many of the outliers have been removed. The stars in the updated catalog have consistent astrometric characteristics. Dashed lines indicate the median for each parameter. Some remaining scatter may be due to measurement errors contamination, and the combination of perspective effects and differences in the Milky Way’s potential varying over the length of Theia 456.

chosen. Our catalog may very well continue to contain some contamination, and it is almost certainly incomplete. In deriving their catalog Kounkel & Covey (2019) made relatively stringent quality cuts, selecting stars with $\varpi/\sigma_\varpi > 10$ and $\sigma_G \lesssim 0.03$ mag, among other constraints. Even within the Gaia catalog there may be more as-yet unidentified Theia 456 members. We show as orange points in Figure 1 the astrometric characteristics of our updated catalog of Theia 456 members; the most significant outliers are removed from this updated sample. We use our updated membership catalog (which we provide in Appendix B) throughout the remainder of this work.

2.2. Kinematic Characteristics

Taking only the orange points and distributions in Figure 1, we find that the stars in our updated Theia 456 membership catalog show a clear overdensity, with median astrometric values: $\mu_\alpha \simeq -4.1 \pm 0.5$ mas yr⁻¹, $\mu_\delta \simeq -1.5 \pm 0.4$ mas yr⁻¹, and $\varpi \simeq 1.9 \pm 0.1$ mas. Although the distribution extends slightly beyond the typical astrometric measurement precision of Gaia EDR3

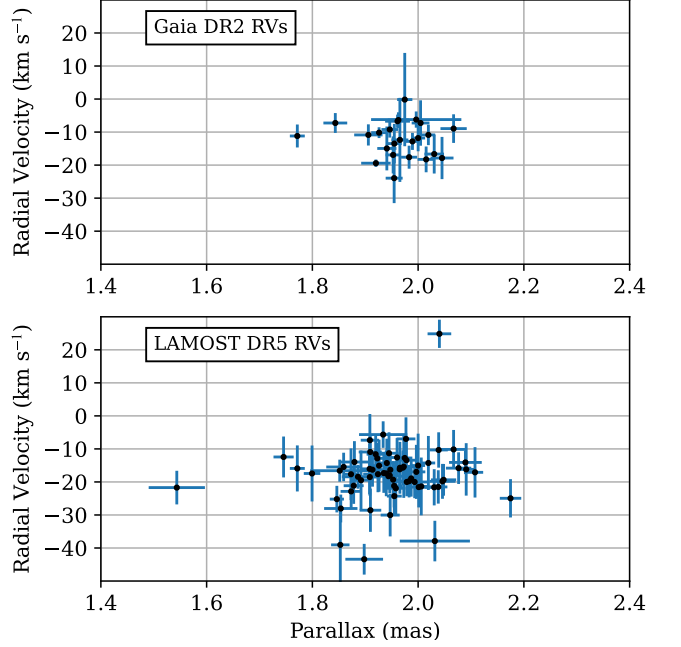


Figure 2. The radial velocities of Theia 456 stars as measured by either Gaia (top panel) or LAMOST (bottom panel) as a function of their Gaia parallaxes. The stars in Theia 456 were identified by their astrometric data only; the overall consistency of the radial velocities provides confirmation that Theia 456 is a kinematically coherent structure.

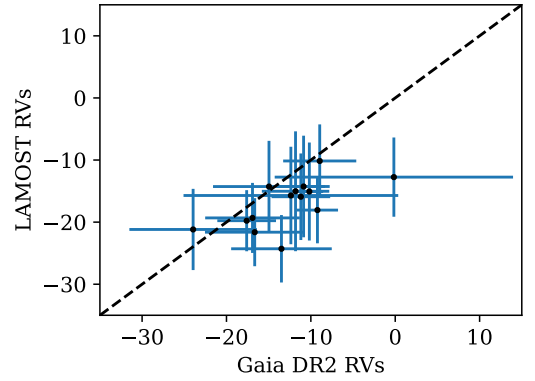


Figure 3. We compare the radial velocities for the 14 stars in Theia 456 which have measurements in both Gaia DR2 and LAMOST. The radial velocities are generally consistent between the two experiments.

(~ 0.1 mas yr⁻¹ in proper motion and ~ 0.02 mas for parallax), some variation is expected for an extended distribution of stars; Theia 456 subtends a large enough angle on the sky that differences in our viewing perspective as well as in the Galactic potential across different ends of the structure can become relevant.

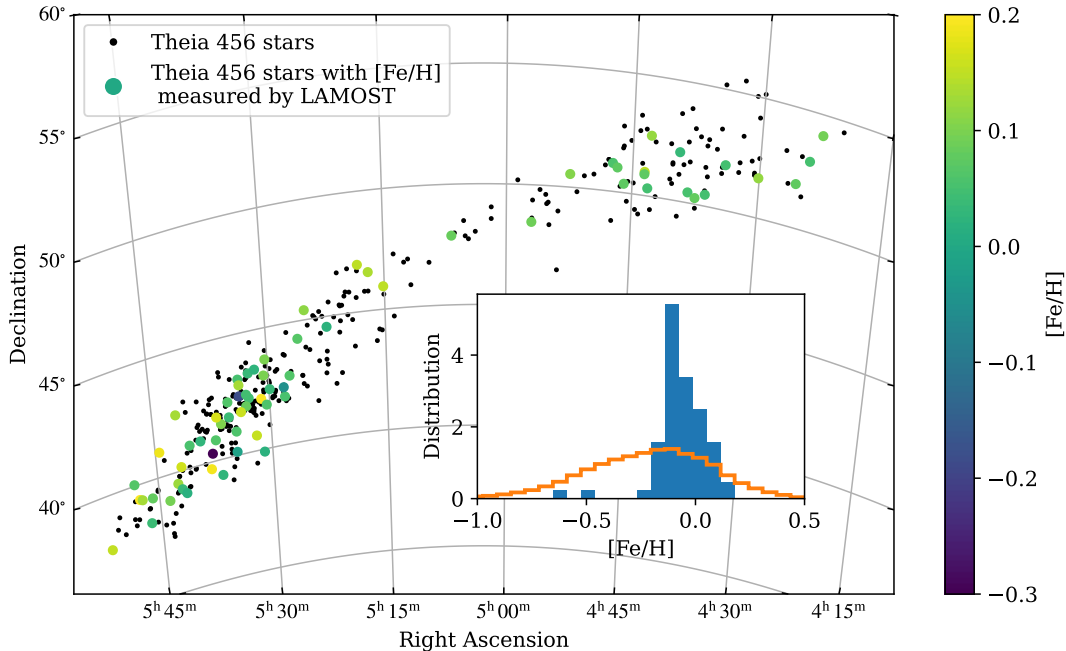


Figure 4. Positions of the 69 stars in Theia 456 with $[\text{Fe}/\text{H}]$ measured by LAMOST (colored markers). Black points indicate the positions of the remaining 293 stars in Theia 456, as identified by Kounkel & Covey (2019). The blue histogram in the inset shows the $[\text{Fe}/\text{H}]$ distribution. With the exception of a few outliers, the stars in Theia 456 are tightly distributed around $[\text{Fe}/\text{H}] = -0.07$ dex. Compared to the orange histogram, which shows the distribution of $[\text{Fe}/\text{H}]$ of all LAMOST stars within the same field of view, Theia 456 stars are sharply concentrated.

Gaia DR2 included radial velocities for seven million stars with $3800 \text{ K} < T_{\text{eff}} < 7000 \text{ K}$ (Katz et al. 2019), measured using the infrared Ca II triplet. For Theia 456 members, these typically have a measurement precision of a few km s^{-1} , depending on the star’s apparent magnitude, stellar type, rotational velocity, and multiplicity. At the same time, the spectroscopic catalog LAMOST has measured radial velocities for a subset of Theia 456 stars, with a precision comparable to that of Gaia. We cross-match our catalog of Theia 456 stars with LAMOST, finding 69 stars with positions in both catalogs matching to within $0.5''$.

In Figure 2, we show these radial velocities for members of Theia 456 as a function of the stars’ Gaia parallax. The Gaia and LAMOST data (24 and 69 stars, respectively) both show a cluster of stars with similar radial velocities (Gaia: $-11.5 \pm 5.3 \text{ km s}^{-1}$; LAMOST: $-17.3 \pm 8.4 \text{ km s}^{-1}$). These are comparable to the median radial velocity measurement precision for Theia 456 members of 5 km s^{-1} for Gaia and 6 km s^{-1} for LAMOST, suggesting that current radial velocity measurements are not precise enough to reliably detect any internal velocity dispersion. A small subset of 14 stars were observed by both instruments, and we compare their respective radial velocity measurements in Figure 3. The two independent radial velocity measurements for these

14 stars are consistent within measurement uncertainties. We note that there appears to be a systematic difference between measurements from the two experiments, consistent with the -5 km s^{-1} offset for LAMOST radial velocities reported by Anguiano et al. (2018) when comparing against radial velocities from APOGEE (Majewski et al. 2017). Whatever offset exists is smaller than typical measurement uncertainties.

The error bars in Figure 2 indicate that, with the exception of a few discrepant points, much of this scatter is likely due to measurement uncertainties. We note that in their algorithm, Kounkel & Covey (2019) did not use radial velocities to identify stellar structures. Furthermore, we did not use radial velocities in producing our refined membership catalog in Section 2.1. The overall radial velocity consistency of stars in Figure 2 serves as a confirmation of the kinematic coherence of Theia 456.

2.3. Metallicity

Figure 4 shows the positions of all the stars in Theia 456, highlighting the subset that have been observed by LAMOST. The LAMOST targets, which are spread out across the length of the stream, tend to have a near-Solar metallicity: their median metallicity is $[\text{Fe}/\text{H}] = -0.07$ dex and a standard deviation of 0.12 dex, with

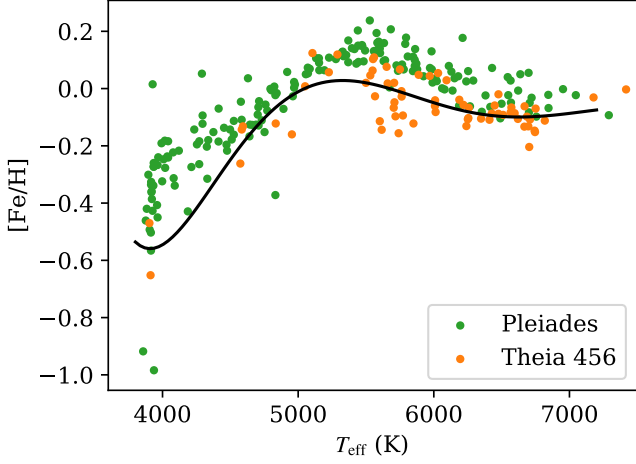


Figure 5. The LAMOST $[\text{Fe}/\text{H}]$ of Pleiads (green) and Theia 456 stars (orange) as a function of the LAMOST-measured T_{eff} . The well-studied Pleiades has been previously shown using high-resolution spectroscopy to have a mean $[\text{Fe}/\text{H}] = +0.01$, with a star-to-star scatter < 0.11 dex (Schuler et al. 2010). Where we would expect to find a consistent $[\text{Fe}/\text{H}]$ throughout the cluster, Pleiads exhibit a systematic trend in LAMOST-measured $[\text{Fe}/\text{H}]$ with respect to T_{eff} , a feature also seen for Theia 456 stars. We also show a seventh order polynomial fit (black line) to Theia 456 stars. Comparing the polynomial fit to our Theia 456 stars gives us an updated dispersion in $[\text{Fe}/\text{H}]$ of 0.07 dex, narrower than the inset to Figure 4 suggests.

the full distribution shown as a blue histogram in the inset of Figure 4.

Typical statistical errors in $[\text{Fe}/\text{H}]$ for LAMOST stars are $\lesssim 0.02$ dex, much smaller than the spread observed in Theia 456 stars. However, repeat measurements by LAMOST of the same stars indicate a somewhat larger uncertainty of $\simeq 0.06$ dex (Luo et al. 2015). By comparing the measured metallicities of stars in widely separated stellar binaries, Andrews et al. (2018) found LAMOST measurements of $[\text{Fe}/\text{H}]$ to be consistent with this somewhat larger measurement precision. For comparison, we note that recent analysis of the Pisces–Eridanus/Meingast 1 stream by Hawkins et al. (2020) indicates a $[\text{Fe}/\text{H}]$ spread of 0.07 dex (most of which is driven by measurement uncertainties), suggesting that the inherent spread one might expect in such a structure should be similar to or smaller than the precision of the LAMOST metallicity measurements.

To look more deeply into LAMOST’s metallicity measurement accuracy, we cross-match the Gaia DR2 sample of Pleiades stars with LAMOST, finding 184 Pleiads with $[\text{Fe}/\text{H}]$ measured by LAMOST. In Figure 5 we compare the T_{eff} with the $[\text{Fe}/\text{H}]$ for these 184 stars as green markers. While previous analysis using high-resolution

spectroscopy (e.g., Schuler et al. 2010) has shown that the Pleiades is co-chemical, with a star-to-star scatter in $[\text{Fe}/\text{H}] < 0.11$ dex, Figure 5 shows a clear systematic dependence in LAMOST data of $[\text{Fe}/\text{H}]$ on T_{eff} . Figure 5 additionally shows these quantities for Theia 456 stars as orange markers. There is a slight offset in the two data sets, consistent with Theia 456 having a lower metallicity. Critically, the dependence of $[\text{Fe}/\text{H}]$ on T_{eff} suggests that the broad distribution of $[\text{Fe}/\text{H}]$ of Theia 456 members (at least compared to the typical measurement uncertainty) is due to a systematic effect in LAMOST $[\text{Fe}/\text{H}]$. As a clear example, the two Theia 456 stars with $T_{\text{eff}} \simeq 4000$ K both have $[\text{Fe}/\text{H}] < -0.4$ dex, corresponding to the low metallicity outliers in the inset of Figure 4.

To derive an improved $[\text{Fe}/\text{H}]$ dispersion, we fit the T_{eff} and $[\text{Fe}/\text{H}]$ for Theia 456 stars to with a seventh order polynomial, which we display in Figure 5 as a black line. Comparison between the polynomial fit and Theia 456 stars provides an updated, de-trended estimate of the $[\text{Fe}/\text{H}]$ dispersion of 0.07 dex, consistent with the magnitude of systematic uncertainties in LAMOST-measured $[\text{Fe}/\text{H}]$ as well as the dispersion previously reported for the Pisces–Eridanus/Meingast 1 stream by Hawkins et al. (2020). Combined with the kinematic coherence described in Section 2.2, we therefore conclude that Theia 456 stars likely have a common origin.

2.4. The challenges of obtaining a robust isochrone age for Theia 456

Isochrone fitting, although not the only approach, has traditionally been the preferred method for dating stellar populations (for a review, see Soderblom 2010). In their catalog Kounkel & Covey (2019) provide an age of $\simeq 165$ Myr for Theia 456, derived from a combination of a bespoke convolutional neural network and a Bayesian Markov chain Monte Carlo method (von Hippel et al. 2006). Despite their complexity, these methods are both based on stellar multi-band photometry, a form of isochrone fitting. Kounkel & Covey (2019) suggest their technique provides an age accuracy of 0.15 dex, which leads to an age range of 115–235 Myr for Theia 456.

Accurate isochrone fitting requires knowledge of the interstellar reddening along the line-of-sight, as fixing the metallicity and reddening is key to obtaining a robust isochrone age. Typically, stellar clusters are either nearby or subtend a small solid angle on the sky, so extinction is minimal or at least constant across the population. Stellar streams present much more of a challenge, as one may need to estimate extinction for each star.

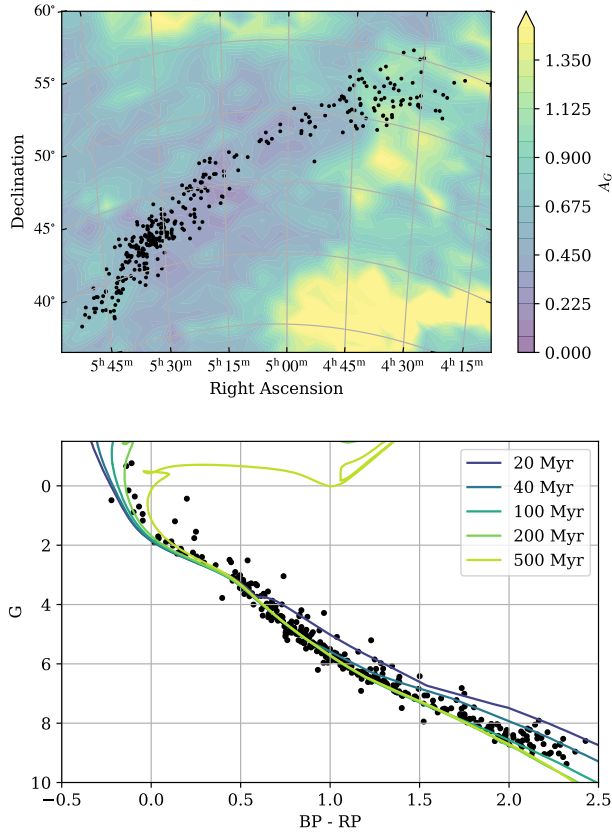


Figure 6. *Top panel*—Positions of Theia 456 stars (black points) overlaid on a dust extinction map compiled from stars at the same distance for which Gaia has measured the A_G . The extinction varies by over a magnitude across the extent of Theia 456. *Bottom panel*— Extinction-corrected color-magnitude diagram for Theia 456 stars. The scatter in the CMD can be due to a combination of effects, including the presence of binaries, contaminating stars, and incorrect extinction estimation. Comparison with isochrones from PARSEC (colored lines) suggest an age of $\simeq 200$ Myr.

Theia 456 spans nearly 25 degrees across the sky and is both sufficiently distant ($\simeq 500$ pc) and sufficiently near the Galactic Plane that the amount of intervening dust could be consequential and vary significantly from star to star. It is therefore worthwhile to revisit the age of Theia 456.

To account for extinction, we generate our own Gaia-based dust map for Theia 456. We select the subset of stars in the field of Theia 456 that have a parallax in the range (1.85, 2.05) mas and for which Gaia has measured a G -band extinction A_G , and perform a k -nearest

neighbors interpolation scheme where $k = 10^1$. The top panel of Figure 6 shows the resulting A_G map and confirms that Theia 456 is a challenging case: the extinction for stars in Theia 456 varies by over a magnitude across its span.

In the bottom panel of Figure 6 we show the resulting color-magnitude diagram (CMD), where we use our dust map to separately account for each star’s extinction and reddening. We used a constant distance of 512 pc in calculating the absolute G magnitudes.² The CMD shows some scatter, more than what is seen in nearby star clusters like the Pleiades or Hyades. Several factors could be contributing to this effect, including contamination, the presence of stellar binaries and blue stragglers, and an imperfect extinction map (Soderblom 2010). Nevertheless, near the turn-off most stars lie close to, or a bit red-ward of, the 200 Myr isochrone (taken from the PARSEC models Bressan et al. 2012), consistent with the 165^{+70}_{-50} Myr age estimate provided by Kounkel & Covey (2019).

2.5. A rotation-based age

Rotation periods provide an additional, robust estimator for stellar ages that is independent of isochrone fitting (Barnes 2007; Mamajek & Hillenbrand 2008). Magnetic braking causes stars of different masses to slow their rotation at different rates. By comparing the photometric colors of the stars in a stellar population with their rotation periods, a clear sequence can be used to determine the stars’ ages. Rather than match theoretical models for stellar spin-down, constraints can be made by comparing to the corresponding distributions in stellar clusters with known ages. Any reasonable comparison requires a large enough sample of stars with high-cadence photometric observations like that provided by surveys from TESS and ZTF.

To obtain this sample, we cross-match the stars in Theia 456 with both photometric surveys, finding 132 and 164 stars have well-sampled photometric data from ZTF and TESS, respectively, with 80 stars sampled by both experiments. Our analysis of these light curves follows that described in detail elsewhere (e.g., Curtis et al. 2020). Briefly, we use an automated pipeline that applies a Lomb-Scargle periodogram to these light curves to derive rotation periods. After visual inspection to

¹ This parallax range is chosen based on the median Theia 456 member parallax of 1.95 mas.

² This distance is taken from the inverse of the median parallax of Theia 456 stars. While it is unlikely that the structure of Theia 456 lies exactly perpendicular to the Sun, we have found no significant variation in the distances to stars over its extent (see Section 2.6).

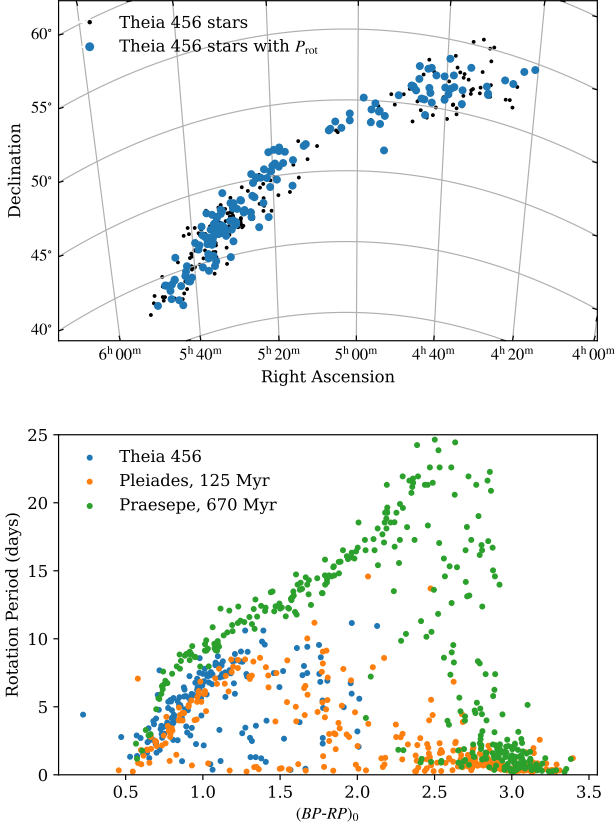


Figure 7. *Top panel*—Theia 456 stars for which we measure a rotation period from either a TESS or a ZTF lightcurve. These stars span the extent of Theia 456. *Bottom panel*—Gaia color–period diagram comparing the distribution for Theia 456 (blue markers) to that of stars from the Pleiades (orange) and Praesepe (green). Theia 456 lies between the Pleiades and Praesepe, suggesting an age between the two.

confirm the quality of these periodicities, we derive robust rotation periods for 216 stars in Theia 456 (see Appendix B for details). For stars with rotation periods measured by both experiments, we use the average.

Crucially, these stars span the full stream (see top panel, Figure 7). The bottom panel of Figure 7 compares the color–rotation period distribution of Theia 456 stars with stars from the Pleiades (125 Myr according to [Stauffer et al. 1998](#), periods from [Rebull et al. 2016](#)) and Praesepe (670 Myr; [Douglas et al. 2019](#)). Three features in the color–period distribution are particularly important for estimating Theia 456’s age. First is the existence of a coherent sequence of slowly rotating stars in the color range $0.5 < (BP - RP) < 1.25$ mag and extending from periods of about a day to periods of about 10 days. The existence of such a sequence indicates that the stream’s stars are indeed coeval, as period measure-

ments for a group of unassociated field stars would not produce such a sequence.

Second is the location of this sequence between those of Pleiades and Praesepe members with the same colors. This suggests that Theia 456’s age is between that of these two benchmark clusters. However, note that this comparison is dependent on accurate de-reddening for the stars in Theia 456. We have separately compared the stellar rotation periods against T_{eff} for those stars observed by LAMOST and found that Theia 456 stars are closely overlapping with the Pleiades.

Third is the turnover of this slow-rotating sequence at a $(BP - RP) \simeq 1.3$. At an older age, such as that of Praesepe, that turnover occurs at redder colors and longer periods (see also the comparison of the Pleiades with M34 by [Stauffer et al. 2016](#)). The similar positioning of the turnover between Theia 456 and the Pleiades suggests the two stellar populations have similar ages.

Combined, our analysis from both isochrone fitting and gyrochronology suggests that the stars in Theia 456 have a common age of 150–200 Myr. A more precise measurement will require a more focused analysis, outside the scope of this work.

2.6. Are There any Gradients across the Extent of Theia 456?

Finally, we search for the existence of any gradients in characteristics across the extent of Theia 456. In particular, Theia 456 appears in Figure 4 to have two wings, one more dense toward the Southeast and one less dense toward the Northwest, with a bridge connecting the two. Using the right ascension as a metric for each member star’s position across the extent of Theia 456, Figure 8 shows how each observable does, or does not, vary. Since Theia 456 spans nearly 20° across the sky, geometric effects cause even two stars moving together to have different proper motions. Therefore, the gradients in μ_α and μ_δ in the top two panels of Figure 8 are expected; we analyze the dynamical history of Theia 456 in Section 3.

The third panel of Figure 8 shows a slight gradient in the parallax across the extent of Theia 456, suggesting the structure may lie at an angle to the Sun, rather than perpendicular. However, a Spearman’s ρ correlation coefficient assigns only a marginal significance to this gradient, with a p -value of 0.06. Therefore, we cannot reject the null hypothesis that no correlation exists. A more dedicated analysis of the membership of Theia 456 will either confirm this gradient or alternatively could find that the slight observed gradient is due to some contamination in the sample at low right ascensions. In the bottom two panels of Figure 8, we show the radial veloc-

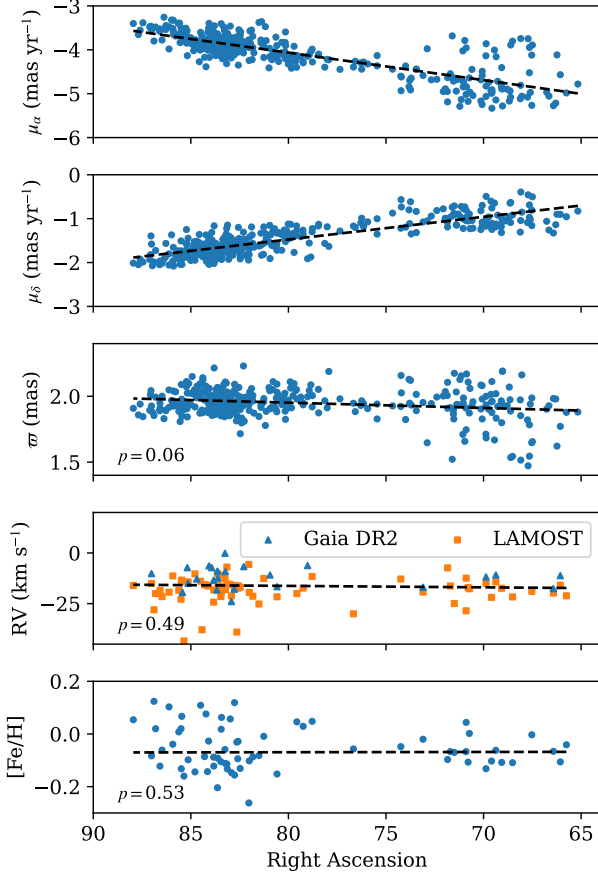


Figure 8. We search for gradients in observables along the extent of Theia 456. Clear gradients exist in proper motion, as expected from geometric effects. p -values (calculated using Spearman’s rank correlation) listed in the bottom left corner of the remaining three quantities (parallax, radial velocity, and $[\text{Fe}/\text{H}]$) indicate the null hypothesis cannot be rejected, and we therefore conclude that no significant correlations exist.

ities and $[\text{Fe}/\text{H}]$ measurements as a function of right ascension. p -values listed in the bottom left corner of each of these panels indicates the lack of a gradient in either of these quantities. We therefore conclude, at least with our current Theia 456 membership catalog and measurement precision, the chemical characteristics of Theia 456 are consistent across its entire extent.

3. DYNAMICAL ORIGIN

Gaia astrometry provides five of the six dimensions of phase space for stars in Theia 456. With the addition of radial velocities from either Gaia DR2 or LAMOST, we can track the motion of a subset of Theia 456 stars backward in time. We use the python package `gala` (Price-Whelan 2017) to integrate the motion of these stars around the Milky Way’s gravitational po-

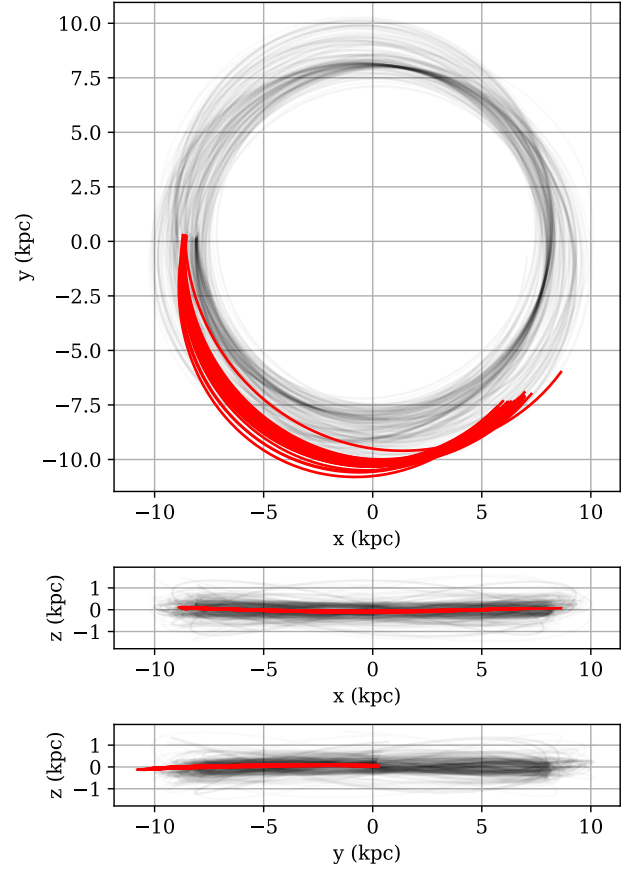


Figure 9. We follow the orbit for 100 Myr backwards in time for the Theia 456 stars with radial velocities measured by Gaia (red). Compare with the orbits of 100 random Gaia DR2 disk stars (black). With its low z -height and low eccentricity, Theia 456 is part of the Milky Way thin disk population.

tential. Integrations are performed within the built-in `MilkyWayPotential` potential using `Astropy` v4.0 defaults (Astropy Collaboration et al. 2013, 2018), which combines an NFW halo potential (Navarro et al. 1997) with the disk model from Bovy (2015). Figure 9 shows the backwards trajectory of these stars (red lines) over the past 100 Myr. Compared with randomly chosen Gaia disk stars (gray lines), the top panel (face-on) and bottom two panels (edge-on, from each side) shows that Theia 456 is clearly part of the Milky Way’s thin disk.

Compared with the positions of Theia 456 stars today (near $y = 0$), the positions our calculations derive for these stars 100 Myr in the past are distributed over several kpc. One may be tempted to conclude that these stars lack a common dynamical origin; however, we find the spread in the ending positions of our orbital integration is due to measurement imprecision. For instance,

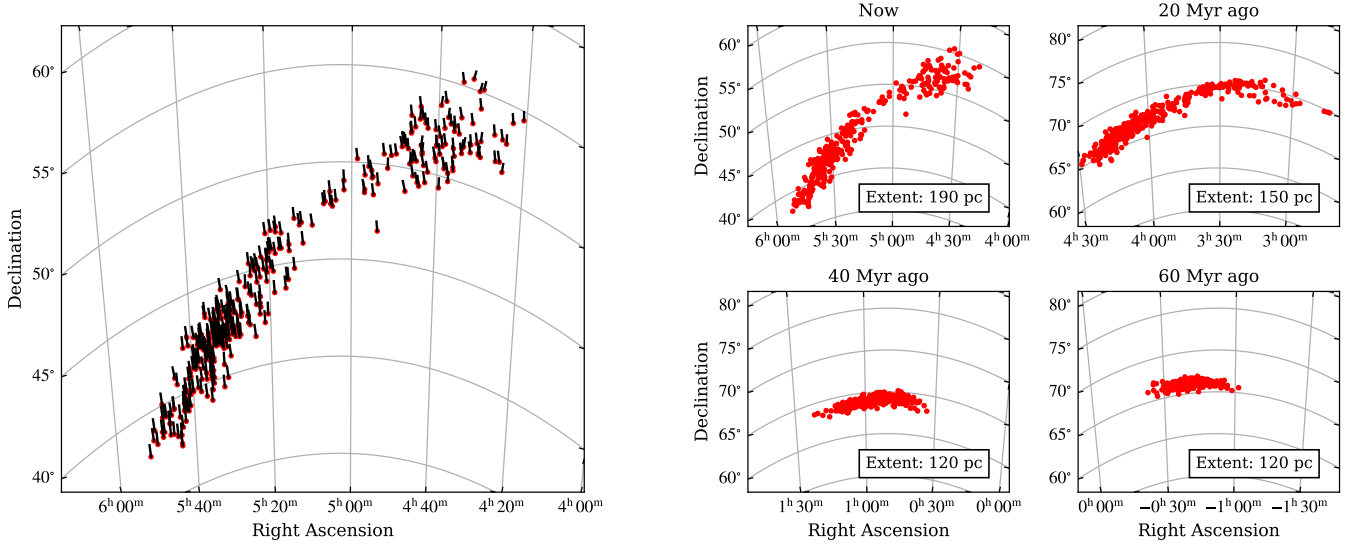


Figure 10. The current positions of Theia 456 members, with lines indicating their proper motions (left panel). The positions of stars are integrated backwards in a Milky Way potential, assuming all stars have a radial velocity of -12.09 km s^{-1} , then mapped onto the sky, accounting for the Sun’s motion around the Milky Way. The right four panels show that the structure appears more compact further back in time. Although some of this effect is due to the fact that Theia 456 was further away from the Sun in the past, we list the spatial extent of Theia 456 in the bottom right of each panel. When integrating backwards, the two ends of Theia 456 appear to have a common origin in a more compact structure.

an imprecision of 1 km s^{-1} in the radial velocity translates to a spread of 100 pc in distance when traveling in a flat gravitational potential. When placed in a Milky Way potential, the combination of these measurement imprecisions and parallactic differences can easily lead to $\sim \text{kpc}$ differences in the calculated positions after 100 Myr. If one wants to exactly calculate the dynamical evolution of the stars in Theia 456, back to their birth 150–200 Myr ago, more precise radial velocities and parallaxes are required. Of course, an accurate model of both the Milky Way potential and the Sun’s phase-space position is required to calculate the exact birth location of Theia 456 stars. Furthermore, clumpiness in the Milky Way potential due to spiral arms, the Milky Way bar, and passing globular clusters and giant molecular clouds is extremely difficult to model and can potentially have a profound impact on the structure of stellar groups (Gieles et al. 2006; Gustafsson et al. 2016; Price-Whelan et al. 2016; Kamdar et al. 2021). However, we are more interested in the shape and spread of the distribution of Theia 456 stars at formation, which is somewhat less sensitive to Milky Way substructure, rather than the exact birth locations of Theia 456 stars.

Nevertheless, we can approximate the backward evolution by repeating the orbital integration while adopting a constant radial velocity of -11.5 km s^{-1} for each star in Theia 456 based on the median Gaia DR2 radial velocity of the stars where it is measured. This approximation

allows us to estimate the prior dynamical evolution of all Theia 456 stars, not just of those with measured radial velocities. The left panel of Figure 10 shows the sky positions of all Theia 456 stars today, with attached lines indicating their proper motion vectors backward in time. In the right four panels, we progressively integrate the orbits further back in time to show how the sky positions of Theia 456 stars changed; we find that 60 Myr ago the stars in Theia 456 contracted into a more compact structure on the sky. At every time step, we additionally calculate the physical extent of the structure, listed in the bottom right of the four righthand panels. One can see from the sky positions of these stars that the two wings to Theia 456 move closer together, a trend confirmed by the smaller size of the cluster in the past. Note that the compactness we observe is dependent upon our adoption of a constant radial velocity for all stars in Theia 456, a significant simplifying approximation. An improved dynamical analysis will require radial velocities with precision $< 1 \text{ km s}^{-1}$ (Ducourant et al. 2014; Donaldson et al. 2016; Crundall et al. 2019).

4. DISCUSSION AND CONCLUSIONS

We have carefully analyzed the membership, kinematics, metallicity, rotation periods, and dynamical origin of Theia 456, one of the several thousand Theia structures identified by Kounkel & Covey (2019) and Kounkel et al. (2020) in Gaia DR2. We produce a more robust

membership catalog of 362 stars. We further confirm the kinematic coherence of these stars, analyzing both the astrometric parameters provided by Gaia and radial velocities provided by both Gaia and LAMOST. Using $[\text{Fe}/\text{H}]$ values measured by LAMOST, we find that Theia 456 stars have similar, slightly sub-solar iron abundances of $[\text{Fe}/\text{H}] = -0.07 \pm 0.12$ dex, with the scatter dominated by systematics in the LAMOST $[\text{Fe}/\text{H}]$ measurements. After carefully analyzing the $[\text{Fe}/\text{H}]$ data, we conclude that Theia 456 stars have a common metallicity.

We additionally cross-match the Theia 456 catalog with ZTF and TESS photometric catalogs, allowing us to find photometric rotation periods for 216 stars. Comparing these to other known stellar populations with well-measured rotation periods and well-constrained ages, we estimate that Theia 456 has an age of 150–200 Myr. This is consistent with the 165^{+70}_{-50} Myr age Kounkel & Covey (2019) derive using machine learning methods. Differential extinction prevents a more precise estimate through photometry alone.

Taken together, these results strongly suggest that the stars in Theia 456 have a common origin, forming at around the same time from chemically well-mixed material. Is this the result of the monolithic collapse paradigm for star formation (Lada & Lada 2003) in which gas clouds collapse and then are tidally disrupted over hundreds of Myr? Our analysis integrating the orbits of Theia 456 stars within a Milky Way potential suggests it originated in a more compact structure. However, our astrometric measurements are not precise enough to differentiate between whether that structure initially began as a more spherical shape as would have been produced by the monolithic collapse of a molecular cloud or if Theia 456 stars formed out of the hierarchical collapse of a more extended structure (Elmegreen 2002, 2008). Many of the Theia objects connect known open clusters with larger, low-density stellar structures surrounding them (Kounkel & Covey 2019; Kounkel et al. 2020), which could be consistent with both theories, depending on whether those stellar streams are the remnants of tidal stripping of the open clusters or whether the open clusters are simply the most overdense regions of an extended, hierarchically collapsing, filamentary cloud.

Theia 456 itself appears to contain two separate regions, one in the Southeast and one in the Northwest, connected by a bridge. We find no significant difference in the bulk kinematic or metallicity characteristics between the two regions, and our dynamical analysis, summarized by Figure 10, indicates the two regions appear to coalesce in the past. While a further, more detailed analysis of stellar membership is required to confirm the

bimodal structure of Theia 456, we speculate that the mere existence of two separate cores lends credence to a hierarchical formation scenario. A dedicated dynamical analysis, which is outside the scope of this work, is required to confirm that conclusion.

Our analysis of Theia 456 has focused on its origin; the corollary is to ask what will Theia 456 look like in 100 Myr. Our astrometric measurements currently lack the precision to accurately integrate the orbits of these stars too far into the future. Nevertheless, we can predict that the combination of the Galactic tide, dynamical motions internal to Theia 456, and passing Milky Way substructures—both dark matter and baryonic—will progressively disrupt the coherency of Theia 456. It seems inevitable that at some point in the future, possibly only ~ 100 Myr hence, Theia 456 will be undiscoverable. We therefore speculate that some fraction of the disk stars comprising the Milky Way, perhaps even the Sun itself, formed in a loosely associated structure like that of Theia 456. Future Gaia data releases, with their improved parallax and proper motion measurements will aid with both confirming the nature of Theia structures as well as identifying new, as-yet undiscovered associations.

While our analysis suggests that the majority of stars identified as Theia 456 share a common origin, follow-up observations providing detailed chemical abundances can be used to further confirm its co-chemical and co-eval nature. If, in fact, such analysis confirms that the stars in this and other Theia objects have a common origin, these will become essential to addressing unsolved problems ranging from planet formation and evolution to the dependence on age of fundamental stellar properties. These questions are best addressed by studying single-age stellar populations, but we have been limited by the relatively small number of known, accessible stellar structures in the solar neighborhood. Theia 456 is just one example of how Gaia is transforming stellar astrophysics.

ACKNOWLEDGMENTS

We thank the anonymous referee for their careful reading of the manuscript and their insightful suggestions.

We thank Soichiro Hattori for sharing an early version of his TESS causal pixel modeling code, `tess_cpm`, prior to its first official release as `unpopular` (Hattori et al. 2021). We measured periods from the resulting light curves using an interactive tool built by high school students participating in the Science Research Mentoring Program at the American Museum of Natural His-

Table 1. Theia 456 Catalog

Gaia ID	Gaia				LAMOST			ZTF	TESS
	RV	<i>G</i>	<i>BP</i>	<i>RP</i>	RV	[Fe/H]	T_{eff}	P_{rot}	P_{rot}
	(km s ⁻¹)	(mag)	(mag)	(mag)	(km s ⁻¹)		(K)	(days)	(days)
191263006888303360	...	16.64	17.59	15.65	-37.9±6.14	-0.652±0.158	3911±166
208504792317742720	...	15.03	15.56	14.29	8.53	8.13
257811119959501952	...	14.69	15.29	13.94	-14.06
256545856951806720	...	16.18	17.00	15.30	9.57	...
256511011879223296	...	15.13	15.70	14.41	7.80	...
256436696063404416	...	16.66	17.48	15.65	3.87	...
255788396520289792	...	14.76	15.30	14.06	6.75	...
211934199151015936	...	17.34	18.51	16.29	2.06	...
208725416200937856	...	17.50	18.53	16.42
207653869102503808	...	17.83	19.11	16.74

tory: we thank Angeli Pante, Isabella Fraczek, and Linus Brooks for their contribution to that tool.

J.J.A. acknowledges support from CIERA and Northwestern University through a Postdoctoral Fellowship. J.L.C. and M.A.A. acknowledge support for this work from the TESS Guest Investigator program under NASA grant 80NSSC22K0299. J.L.C. acknowledges support provided by the NSF through grant AST-2009840. J.C. acknowledges support from the Agencia Nacional de Investigación y Desarrollo (ANID) via Proyecto Fondecyt Regular 1191366; and from “Centro de Astronomía y Tecnologías Afines” project BASAL AFB-170002. S.C.S. was supported by a Research Innovation and Scholarly Excellence (RISE) grant from the University of Tampa.

This work has made use of data from the European Space Agency (ESA) mission *Gaia*,³ processed by the *Gaia* Data Processing and Analysis Consortium (DPAC).⁴ Funding for the DPAC has been provided by

national institutions, in particular the institutions participating in the *Gaia* Multilateral Agreement.

Guoshoujing Telescope (the Large Sky Area Multi-Object Fiber Spectroscopic Telescope LAMOST) is a National Major Scientific Project built by the Chinese Academy of Sciences. Funding for the project has been provided by the National Development and Reform Commission. LAMOST is operated and managed by the National Astronomical Observatories, Chinese Academy of Sciences.

Software: `astropy` (Astropy Collaboration et al. 2018), `astroquery` (Ginsburg et al. 2019), `gala` (Price-Whelan et al. 2020), `NumPy` (van der Walt et al. 2011), `SciPy` (Jones et al. 2001), `matplotlib` (Hunter 2007), `scikit-learn` (Pedregosa et al. 2011), `TESScut` (Brasseur et al. 2019), `unpopular` (Hattori et al. 2021), The IDL Astronomy User’s Library (Landsman 1993)

APPENDIX

A. CATALOG OF THEIA 456 MEMBERS

We provide a catalog of the 362 members we identify within Theia 456. Table 1 provides a sample of this data, which includes only a subset of the columns for the first 10 members. The complete dataset, which is publicly available, contains all the data from Gaia EDR3, as well as LAMOST data, our derived extinctions for the three Gaia photometric bands, and rotation periods from ZTF and TESS.

B. DETAILS OF THE ROTATION PERIOD ANALYSIS

We measured rotation periods using time series imaging data acquired by the space-based TESS and ground-based ZTF facilities. For TESS, we downloaded 40×40 pixel image cutouts with `TESScut` (Brasseur et al. 2019), then

³ <https://www.cosmos.esa.int/gaia>

⁴ <https://www.cosmos.esa.int/web/gaia/dpac/consortium>

extracted light curves using the TESS causal pixel modeling package `unpopular` (Hattori et al. 2021). Briefly, this tool uses pixels outside of an exclusion region centered on the target (the central 6×6 pixels in our implementation) to model and subtract off the time-varying systematics (e.g., Earthshine reflected into the TESS optics). Next, we calculate Lomb–Scargle periodograms (Lomb 1976; Scargle 1982; Press & Rybicki 1989) with `astropy.timeseries` with test periods spaced logarithmically between 0.1 and 30 days. We visually inspected the light curves, periodograms, and phase-folded light curves to select the optimal sectors or segments of data to use, identify cases where the periodogram preferred the 1/2-period harmonic period, and classify the light curve to validate the resulting period.

For ZTF, following the procedure described by Curtis et al. (2020), we downloaded $8' \times 8'$ image cutouts from the NASA/IPAC Infrared Science Archive (IRSA). Next, we extracted light curves using simple aperture photometry for each target and a selection of neighboring stars queried from Gaia. The light curves for the target and references stars are normalized by subtracting off their median magnitudes, and then a systematics light curve (i.e., per epoch zeropoint corrections) is created by calculating the median magnitude of this cohort at each epoch to capture their systematically varying brightnesses. We subtract this systematic signal from the target’s light curve to produce a refined light curve ready for period analysis. Our procedure typically improves the photometric precision over the light curves produced by the ZTF pipeline. We then apply a similar Lomb–Scargle approach to measure rotation periods as was applied to the TESS data.

REFERENCES

- Andrews, J. J., Chanamé, J., & Agüeros, M. A. 2018, *MNRAS*, 473, 5393
- Anguiano, B., Majewski, S. R., Allende Prieto, C., et al. 2018, *A&A*, 620, A76
- Astropy Collaboration, Robitaille, T. P., Tollerud, E. J., et al. 2013, *A&A*, 558, A33
- Astropy Collaboration, Price-Whelan, A. M., Sipőcz, B. M., et al. 2018, *AJ*, 156, 123
- Barnes, S. A. 2007, *ApJ*, 669, 1167
- Beccari, G., Boffin, H. M. J., & Jerabkova, T. 2020, *MNRAS*, 491, 2205
- Bellm, E. C., Kulkarni, S. R., Graham, M. J., et al. 2019a, *PASP*, 131, 018002
- . 2019b, *PASP*, 131, 018002
- Belokurov, V., Erkal, D., Evans, N. W., Koposov, S. E., & Deason, A. J. 2018, *MNRAS*, 478, 611
- Bovy, J. 2015, *ApJS*, 216, 29
- Brasseur, C., Phillip, C., Fleming, S. W., Mullally, S., & White, R. L. 2019, *Astrocute: Tools for creating cutouts of TESS images*, , ascl:1905.007
- Bressan, A., Marigo, P., Girardi, L., et al. 2012, *MNRAS*, 427, 127
- Bressert, E., Bastian, N., Gutermuth, R., et al. 2010, *MNRAS*, 409, L54
- Campello, R. J. G. B., Moulavi, D., & Sander, J. 2013, in *Advances in Knowledge Discovery and Data Mining*, ed. J. Pei, V. S. Tseng, L. Cao, H. Motoda, & G. Xu (Berlin, Heidelberg: Springer Berlin Heidelberg), 160–172
- Castro-Ginard, A., Jordi, C., Luri, X., et al. 2020, *A&A*, 635, A45
- Crundall, T. D., Ireland, M. J., Krumholz, M. R., et al. 2019, *MNRAS*, 489, 3625
- Cui, X.-Q., Zhao, Y.-H., Chu, Y.-Q., et al. 2012, *Research in Astronomy and Astrophysics*, 12, 1197
- Curtis, J. L., Agüeros, M. A., Mamajek, E. E., Wright, J. T., & Cummings, J. D. 2019, *AJ*, 158, 77
- Curtis, J. L., Agüeros, M. A., Matt, S. P., et al. 2020, *ApJ*, 904, 140
- Donaldson, J. K., Weinberger, A. J., Gagné, J., et al. 2016, *ApJ*, 833, 95
- Douglas, S. T., Curtis, J. L., Agüeros, M. A., et al. 2019, *ApJ*, 879, 100
- Ducourant, C., Teixeira, R., Galli, P. A. B., et al. 2014, *A&A*, 563, A121
- Elmegreen, B. G. 2002, *ApJ*, 577, 206
- . 2008, *ApJ*, 672, 1006
- Fall, S. M., Chandar, R., & Whitmore, B. C. 2005, *ApJL*, 631, L133
- Gaia Collaboration, Brown, A. G. A., Vallenari, A., et al. 2018, *A&A*, 616, A1
- . 2021, *A&A*, 649, A1
- Gieles, M., Portegies Zwart, S. F., Baumgardt, H., et al. 2006, *MNRAS*, 371, 793
- Ginsburg, A., Sipőcz, B. M., Brasseur, C. E., et al. 2019, *AJ*, 157, 98
- Goodwin, S. P., & Bastian, N. 2006, *MNRAS*, 373, 752
- Gustafsson, B., Church, R. P., Davies, M. B., & Rickman, H. 2016, *A&A*, 593, A85
- Hattori, S., Foreman-Mackey, D., Hogg, D. W., et al. 2021, *arXiv e-prints*, arXiv:2106.15063
- Hawkins, K., Lucey, M., & Curtis, J. 2020, *MNRAS*, 496, 2422
- Helmi, A. 2020, *ARA&A*, 58, 205

- Helmi, A., Babusiaux, C., Koppelman, H. H., et al. 2018, *Nature*, 563, 85
- Hunter, J. D. 2007, *Computing in Science Engineering*, 9, 90
- Jones, E., Oliphant, T., Peterson, P., et al. 2001, *SciPy: Open source scientific tools for Python*, .
<http://www.scipy.org/>
- Kamdar, H., Conroy, C., & Ting, Y.-S. 2021, arXiv e-prints, arXiv:2106.02050
- Kamdar, H., Conroy, C., Ting, Y.-S., et al. 2019, *ApJ*, 884, 173
- Katz, D., Sartoretti, P., Cropper, M., et al. 2019, *A&A*, 622, A205
- Kounkel, M., & Covey, K. 2019, *AJ*, 158, 122
- Kounkel, M., Covey, K., & Stassun, K. G. 2020, *AJ*, 160, 279
- Lada, C. J., & Lada, E. A. 2003, *ARA&A*, 41, 57
- Landsman, W. B. 1993, in *Astronomical Society of the Pacific Conference Series*, Vol. 52, *Astronomical Data Analysis Software and Systems II*, ed. R. J. Hanisch, R. J. V. Brissenden, & J. Barnes, 246
- Lindgren, L., Hernández, J., Bombrun, A., et al. 2018, *A&A*, 616, A2
- Lindgren, L., Klioner, S. A., Hernández, J., et al. 2021, *A&A*, 649, A2
- Lomb, N. R. 1976, *Ap&SS*, 39, 447
- Luo, A. L., Zhao, Y.-H., Zhao, G., et al. 2015, *Research in Astronomy and Astrophysics*, 15, 1095
- Majewski, S. R., Schiavon, R. P., Frinchaboy, P. M., et al. 2017, *AJ*, 154, 94
- Mamajek, E. E., & Hillenbrand, L. A. 2008, *ApJ*, 687, 1264
- McInnes, L., Healy, J., & Astels, S. 2017, *The Journal of Open Source Software*, 2, 205
- Meingast, S., Alves, J., & Fürnkranz, V. 2019, *A&A*, 622, L13
- Navarro, J. F., Frenk, C. S., & White, S. D. M. 1997, *ApJ*, 490, 493
- Odenkirchen, M., Grebel, E. K., Rockosi, C. M., et al. 2001, *ApJL*, 548, L165
- Pedregosa, F., Varoquaux, G., Gramfort, A., et al. 2011, *Journal of Machine Learning Research*, 12, 2825
- Press, W. H., & Rybicki, G. B. 1989, *ApJ*, 338, 277
- Price-Whelan, A., Sipőcz, B., Lenz, D., et al. 2020, *adrn/gala: v1.3, vv1.3*, Zenodo,
doi:10.5281/zenodo.4159870.
<https://doi.org/10.5281/zenodo.4159870>
- Price-Whelan, A. M. 2017, *The Journal of Open Source Software*, 2, 388
- Price-Whelan, A. M., Sesar, B., Johnston, K. V., & Rix, H.-W. 2016, *ApJ*, 824, 104
- Ratzenböck, S., Meingast, S., Alves, J., Möller, T., & Bomze, I. 2020, *A&A*, 639, A64
- Rebull, L. M., Stauffer, J. R., Bouvier, J., et al. 2016, *AJ*, 152, 113
- Renaud, F., Bournaud, F., Emsellem, E., et al. 2013, *MNRAS*, 436, 1836
- Ricker, G. R., Winn, J. N., Vanderspek, R., et al. 2015, *Journal of Astronomical Telescopes, Instruments, and Systems*, 1, 014003
- Riello, M., De Angeli, F., Evans, D. W., et al. 2021, *A&A*, 649, A3
- Röser, S., & Schilbach, E. 2020, *A&A*, 638, A9
- Scargle, J. D. 1982, *ApJ*, 263, 835
- Schuler, S. C., Plunkett, A. L., King, J. R., & Pinsonneault, M. H. 2010, *PASP*, 122, 766
- Soderblom, D. R. 2010, *ARA&A*, 48, 581
- Stauffer, J., Rebull, L., Bouvier, J., et al. 2016, *AJ*, 152, 115
- Stauffer, J. R., Schultz, G., & Kirkpatrick, J. D. 1998, *ApJL*, 499, L199
- Tian, H.-J. 2020, *ApJ*, 904, 196
- Ujjwal, K., Kartha, S. S., Mathew, B., Manoj, P., & Narang, M. 2020, *AJ*, 159, 166
- van der Walt, S., Colbert, S. C., & Varoquaux, G. 2011, *Computing in Science Engineering*, 13, 22
- van Loon, J. T., Gilmore, G. F., Omont, A., et al. 2003, *MNRAS*, 338, 857
- Vitral, E. 2021, *MNRAS*, 504, 1355
- von Hippel, T., Jefferys, W. H., Scott, J., et al. 2006, *ApJ*, 645, 1436